PHYSICAL REVIEW FLUIDS **10**, 084703 (2025)

Extreme vortex-gust airfoil interactions at Reynolds number 5000

Kai Fukami [*]
Department of Aerospace Engineering, Graduate School of Engineering, Tohoku University, Sendai, 980-8579, Japan

Luke Smith
Texas Advanced Computing Center, University of Texas at Austin, Austin, Texas 78758, USA

Kunihiko Taira
Department of Mechanical and Aerospace Engineering, University of California, Los Angeles, California 90095, USA

(Received 15 April 2025; accepted 8 July 2025; published 12 August 2025)

We study interactions between an NACA0012 airfoil and a discrete vortex gust of extreme strength at a chord-based Reynolds number of 5000. This paper considers the gust ratios of $G \geqslant 1$, representative of conditions experienced by small-scale aircraft in adverse flight environments. We first carry out large-eddy simulations of spanwise periodic flows around an airfoil at the angle of attack of 14°, exhibiting a turbulent separated wake. Introducing a vortex gust as a Taylor vortex upstream of the wing, the dependence of aerodynamic forces and vortical flows on gust parameters such as magnitude, rotational direction (positive and negative signs), size, and orientation is investigated. The lift responses and flow fields exhibit primarily two-dimensional behavior up to the gust ratio $|G|$ of 3, while three-dimensionality with very fine-scale structures emerges for $|G| \geqslant 4$, triggering instabilities during the interaction. Once the gust becomes large in size, the fluctuation of aerodynamic loads is further enlarged, and the deformation of vortical flows and lift response is experienced earlier compared with cases with a small-sized gust, which reveals the dangerous aerodynamic situation hindering stable flights. The current study also shows that the fluctuation of the unsteady lift strongly depends on the gust location and rotational direction, providing hints for lift attenuation. Scale-decomposition analysis is performed to further examine the energy-transfer dynamics in extreme vortex-airfoil interaction across a range of spatial length scales. We reveal that the energy from large-scale vortex cores is transferred to the shear layers that emerge due to the interaction. Based on the current findings, we also consider unsupervised machine learning-based data compression of the present extreme vortex-gust airfoil interactions with an observable-augmented nonlinear autoencoder. A collection of vortical flow snapshots for $|G| \leqslant 3$ whose interaction dynamics are primarily two-dimensional can be compressed to three variables while extracting the important vortical structures associated with the lift coefficient. The findings throughout this study suggest that modeling and control strategies developed for two-dimensional problems could be considered for analyzing extreme vortex-airfoil interactions at higher Reynolds numbers.

DOI: 10.1103/vcbd-tvz1

[*]Contact author: kfukami1@tohoku.ac.jp

I. INTRODUCTION

Modern small- and medium-sized aircraft are increasingly tasked to operate in aerodynamically challenging environments, including airspace in urban canyons, over mountainous terrain, and behind ships. In such adverse situations, they encounter extremely unsteady flows where the spatiotemporal scales of disturbances are nearly the same or larger in magnitude compared with the flight speed [1]. This study examines the effect of extremely strong vortex disturbance on aerodynamic responses of flows around an airfoil through numerical simulations and data-driven analysis.

In studying vortex-gust airfoil interactions, vortex disturbance is characterized by various parameters, such as vortex strength, size, and orientation [2]. Among them, the gust ratio $G \equiv u_g/u_\infty$ is particularly important, where u_g is the characteristic gust velocity and u_∞ is the freestream velocity. This value is generally quite low for large-scale aircraft due to their high cruise velocity u_∞. However, G becomes large for small-scale aircraft, such as drones, due to its low cruise velocity, even for the same u_g.

As flight conditions of $G \geqslant 1$ have been traditionally considered unflyable, the primary concern in previous studies of vortex-gust airfoil interactions has been focused on cases with $G < 1$. For instance, Qian *et al.* [3] performed experimental investigations into vortex-gust interactions with an airfoil under conditions of $G \leqslant 0.5$. Through Particle Image Velocimetry (PIV) measurements, they explored the influence of parameters such as gust ratio, angle of attack, and wing sweep angle on vortical structures and aerodynamic forces. Herrmann *et al.* [4] proposed a proportional-integral feedback/model-based feedforward control to relieve the impact of gusts with $G \leqslant 0.1$ on flows around a DLR-F15 airfoil, achieving a 64% reduction in the lift fluctuation during quasirandom gust encounters. A closed-loop pitch control for mitigation of lift deviation due to transverse gust encounters was also examined by Sedky *et al.* [5] for conditions of $G \leqslant 0.71$. At a high Reynolds number of $\mathrm{Re} = 200\,000$ for $G = 0.5$, Barnes and Visbal [6,7] performed large-eddy simulations (LESs) of interactions between a vortex gust and an NACA0012 airfoil to investigate the dependence of flow behaviors on the rotational direction and orientation of gusts against a wing. Furthermore, some unsupervised learning techniques and time-dependent modal analyses have been considered in studying the nonlinear and transient nature of gust airfoil interactions of $G < 1$ [8,9].

Recent studies have explored conditions of $G \geqslant 1$ that can emerge in urban canyons, mountainous environments, and severe atmospheric turbulence for small-scale air vehicles [10]. Moushegian *et al.* [11] performed a delayed detached eddy simulation of transverse gust encounter with $G = 1$ while comparing it to the Küssner linear gust theory and PIV measurements. Biler *et al.* [12] experimentally investigated the lift response of transverse and vortex gust encounters with $0.5 \leqslant G \leqslant 1.5$. They reported that the Helmbold equation can be used to predict the lift coefficient based on the gust-induced angle of attack. Effects of transverse gust velocity profiles on aerodynamic responses for $0.5 \leqslant G \leqslant 1.5$ are also comprehensively examined by Andreu-Angulo *et al.* [13] with their top hat gust generator. A recent experimental study by Andreu-Angulo and Babinsky [14] has explored the dependence of the sign of transverse gusts on lift mitigation by pitching control for $G = 0.5$ and 1, providing a comprehensive analysis of the relationship between an effective angle of attack and vortical motions.

For extremely high levels of vortex disturbance with $0 < G \leqslant 10$, our recent study [15] showed that time-varying two-dimensional vortical flow field data spanning the large-parameter space can be compressed to only three variables with nonlinear unsupervised learning. The proposed technique, called an observable-augmented autoencoder, finds a low-dimensional manifold that captures the influence of extreme vortex disturbance on the baseline flow dynamics. In the study [15], we refer to aerodynamics with $G \geqslant 1$ as *extreme aerodynamics* due to the presence of violently strong gusts. Following the discovery of the low-order manifold, follow-up studies have further shown that such data-driven low-order representations can be used to design optimal control strategies to swiftly mitigate the impact of vortex disturbances, equipped with phase-amplitude modeling [16] and reinforcement learning [17].

TABLE I. The parameter list considered in the present study.

Case ID	G	D	Y	Case ID	G	D	Y	Case ID	G	D	Y	Case ID	G	D	Y	Case ID	G	D	Y
1	0.5	0.5	0.1	6	5	0.5	0.1	11	−4	0.5	0.1	16	−2	0.5	−0.3	21	−2	1.5	0.1
2	1	0.5	0.1	7	−0.5	0.5	0.1	12	−5	0.5	0.1	17	2	1.0	0.1	22	−2	2.0	0.1
3	2	0.5	0.1	8	−1	0.5	0.1	13	2	0.5	−0.1	18	2	1.5	0.1				
4	3	0.5	0.1	9	−2	0.5	0.1	14	2	0.5	−0.3	19	2	2.0	0.1				
5	4	0.5	0.1	10	−3	0.5	0.1	15	−2	0.5	−0.1	20	−2	1.0	0.1				

While there exist a few studies focusing on $G \geqslant 1$, their analyses are limited to low-Reynolds-number simulations or experiments that produce sectional measurements only, necessitating comprehensive examinations of higher Reynolds number flow. In response, this study considers extreme vortex-airfoil interactions, with an interest in their behaviors across a spanwise periodic domain. We first perform LESs of flows around an NACA0012 airfoil at a chord-based Reynolds number of 5000, encountering a violent gust vortex of $G \geqslant 1$. Strongly disturbed flows are then examined with respect to aerodynamic forces and vortical flows while varying gust parameters, such as magnitude, size, rotational direction (positive and negative signs), and orientation. Along with the current findings from numerical simulations, we further consider nonlinear autoencoder-based data compression of the present vortex-gust airfoil interactions, providing insights into understanding and modeling for extreme aerodynamic flows at a range of Reynolds numbers.

This paper is organized as follows. The present simulation setup is described in Sec. II. Results produced by the simulations and data-driven analyses are presented in Sec. III. Conclusions are offered in Sec. IV.

II. SIMULATION SETUP

We perform LESs of an NACA0012 airfoil at a chord-based Reynolds number $\mathrm{Re} = u_\infty c/\nu = 5000$, where c is the chord length and ν is the kinematic viscosity. The angle of attack α is set to 14°, producing a turbulent separated wake. We perform LES using an incompressible flow solver *Cliff* (in *CharLES* software package) based on the finite-volume formulation with second-order accuracy in time and space [18,19]. The computational domain is set over $(x, y, z)/c \in [-20, 25] \times [-20, 20] \times [0, 1]$, with the leading edge of the wing positioned at the origin. The inlet and far-field boundaries are prescribed with freestream, while the convective boundary condition is applied at the outlet. The no-slip boundary condition is imposed on the wing surface. The present LES with spanwise extent of $1c$ is performed over a spanwise periodic domain that captures the three-dimensional flow structures [20,21]. The Vreman subgrid-scale model [22] is used to provide turbulent closure for the present LES.

For the disturbed flows, a strong vortex gust is introduced upstream of an airfoil at $x_0/c = -2$. The disturbance is modeled with a Taylor vortex [23] whose rotational velocity profile is determined as

$$u_\theta = u_{\theta,\max} \frac{r}{R} \exp\left[\frac{1}{2}\left(1 - \frac{r^2}{R^2}\right)\right], \tag{1}$$

where R is the radius at which u_θ reaches its maximum velocity $u_{\theta,\max}$. In the present analysis, the effect of the vortex gust on aerodynamic responses is examined by sweeping the parameters of the gust ratio $G \equiv u_{\theta,\max}/u_\infty \in [-5, 5]$, its size $D \equiv 2R/c \in [0.5, 1.5]$, and vertical position of the disturbance $y_0/c \equiv Y \in [-0.3, 0.3]$ relative to the wing, as summarized in Table I. We again note that the present gust ratio magnitude $|G|$ is much larger than 1.

The grid dependence with respect to the vortical flow structures and lift forces is examined by considering three different spatial resolutions: regular ($\approx 8 \times 10^6$), fine ($\approx 20 \times 10^6$ with the domain presented in Fig. 1), and finer ($\approx 40 \times 10^6$). The comparison of flow fields and aerodynamic forces

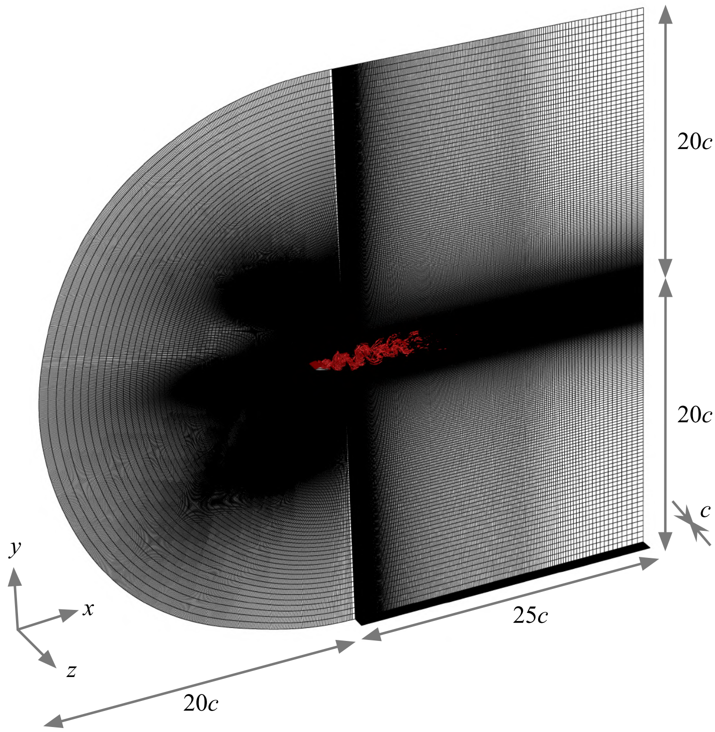

FIG. 1. The computational domain with a fine grid mesh ($\approx$20 $\times$ 10^6 cell counts).

for the undisturbed flow among the meshes and previous studies [21,24] is shown in Fig. 2. Here, the lift coefficient and the drag coefficient are defined as $C_L \equiv F_L/(0.5\rho u_\infty^2 c)$ and $C_D \equiv F_D/(0.5\rho u_\infty^2 c)$, respectively, where F_L and F_D are the lift and drag forces on the wing body and ρ is the density. Since the results show convergence, we choose the fine mesh to compute the undisturbed flow. We further compare these grids for a disturbed flow with $(G, D, Y) = (1, 0.5, 0.1)$, as presented in Fig. 3. Here, the convective time nondimensionalized by (c/u_∞) is set to zero when the center of the vortex arrives at the leading edge of the wing. While the lift response does not show significant differences across the grid resolution, its effect is slightly observed for the evolution of vortical

(a)

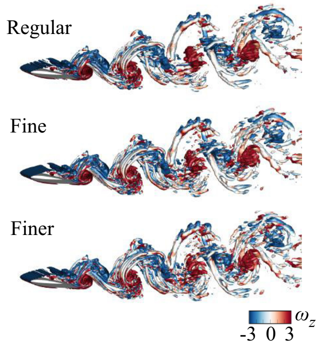

(b)

		$\overline{C_L}$	$C_{L,\,\mathrm{rms}}$	$\overline{C_D}$	$C_{D,\,\mathrm{rms}}$	L_z/c	Note
Present	Regular (8M)	0.730	0.103	0.245	0.0224	1	—
Present	Fine (20M)	0.737	0.116	0.249	0.0190	1	—
Present	Finer (40M)	0.738	0.098	0.249	0.0183	1	—
	Rolandi *et al.* (2025)	0.734	—	0.246	—	1	LES ($M_\infty = 0.2$)
	Gupta *et al.* (2023)	0.763	—	0.223	—	10	Wind-tunnel experiment

FIG. 2. (a) Comparisons of an instantaneous baseline flow visualized by isocontours of Q-criterion. (b) Comparisons of lift and drag forces (time-averaged value and root-mean-squared value).

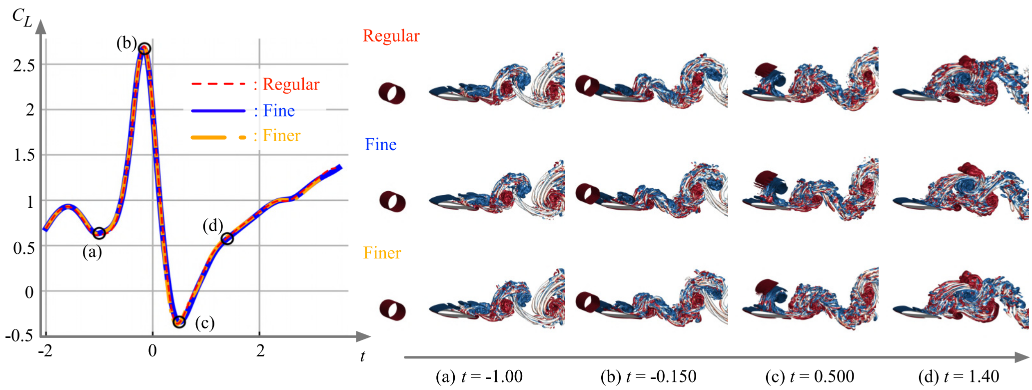

FIG. 3. The lift coefficient C_L and vortical flow visualized by the isocontours of Q-criterion across the three grid resolutions over time.

structures, especially downstream, as seen in Fig. 3(d). Following the impact of the gust on the wing, the downstream convection of vortex structures differs slightly between the regular and fine cases, likely due to mesh coarseness in the region far from the wing. Along with our verification for the undisturbed case, we hereafter use the fine grid for the present study.

III. RESULTS

A. Vortical flow fields and lift response for $|G| \leqslant 3$

We examine the flow fields and lift force from the present LES. Let us begin with the undisturbed baseline flow, as summarized in Fig. 4. At the current chord-based Reynolds number of 5000 with $\alpha = 14^\circ$, the flow is fully separated over the wing. The shear layer separating from the leading edge rolls up over the wing, forming two-dimensional vortical structures associated with the Kelvin-Helmholtz instability. As the wake evolves, these vortical structures break down, producing three-dimensional structures in the wake. Although this turbulent wake possesses three-dimensional rib structures around shear layers related to the mode C instability [25], the primary feature remains two-dimensional, as exhibited in the spanwise-averaged spanwise vorticity field in Fig. 4(a). Since the current study considers a two-dimensional wing profile, the present baseline flow at $\alpha = 14^\circ$ is a representative model case to examine the effect of three-dimensionality caused by the spanwise extent and Reynolds number in extreme vortex-airfoil interactions. The time trace and spectra of lift coefficient C_L are also shown in Figs. 4(b) and 4(c), respectively. Here, the frequency f is nondimensionalized by (u_∞/c). Corresponding to the coherent vortex shedding observed in Fig. 4(a), the lift oscillates over time while exhibiting quasiperiodicity, which is also evident from the notable peak in the lift spectra. The current problem setup serves as a canonical study in examining gust effects on unsteady flight operations.

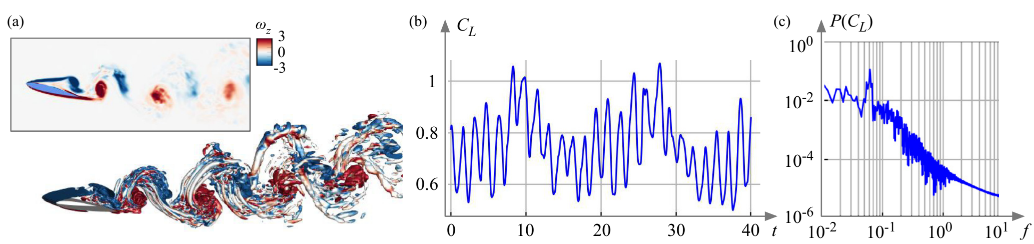

FIG. 4. The undisturbed baseline flow. (a) Instantaneous three-dimensional flow field visualized by the isocontours of Q-criterion and spanwise-averaged spanwise vorticity field ω_z. (b) Time series and (c) spectra of lift coefficient C_L.

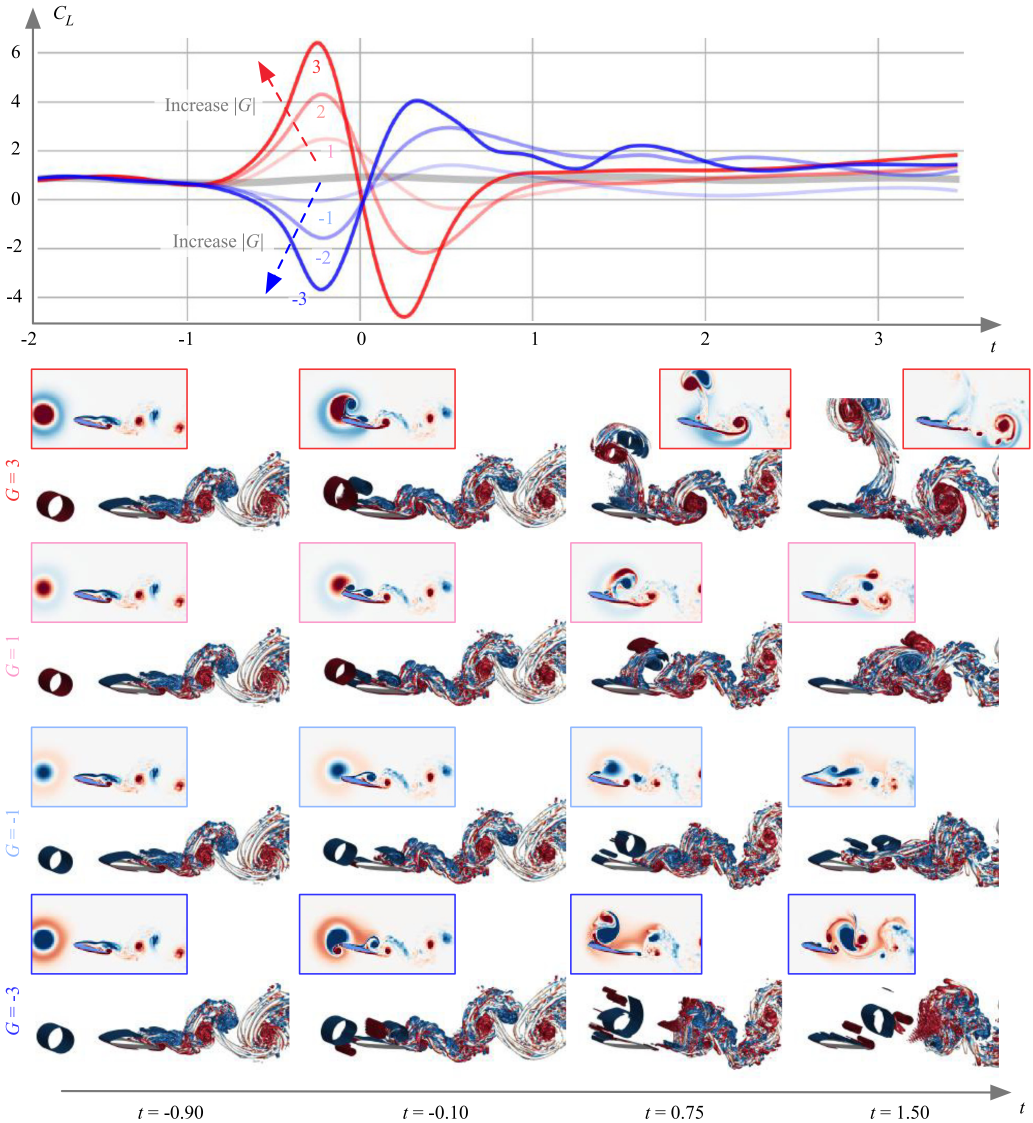

FIG. 5. Dependence of lift coefficient C_L and flow field on the gust ratio G. Three-dimensional flow fields visualized by the isocontours of Q-criterion and spanwise-averaged spanwise vorticity fields ω_z are presented over time. The cases for $(D, Y) = (0.5, 0.1)$ with $G = [-3, 3]$ are shown. The gray line in the lift response corresponds to the undisturbed case.

1. *The effect of gust ratio G*

Next, let us discuss the disturbed flows. Since the gust ratio G influences the flyability of modern small-sized aircraft, the effect of G on lift coefficient C_L and flow field for cases of $(D, Y) = (0.5, 0.1)$ is first examined in Fig. 5. As representative examples, the cases with $G = [-3, 3]$ are considered. The fluctuation from the undisturbed lift coefficient increases as $|G|$ becomes large. Correspondingly, the separation also becomes massive—for example, the impinging vortex gust removes almost all structures near the wing with $G = 3$ at $t > 0.75$.

When a positive vortex gust approaches the wing, the lift first increases from the undisturbed state. Once this positive gust impinges on the wing, the violent interaction between the gust and

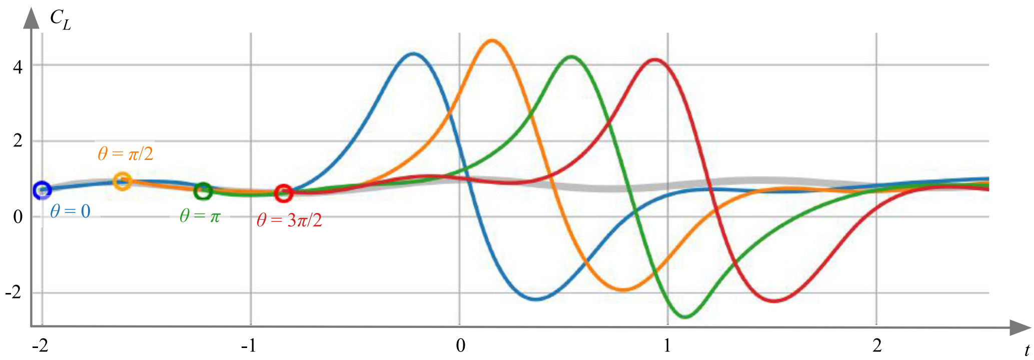

FIG. 6. Dependence of lift coefficient C_L on the timing introducing a gust with $(G, D, Y) = (2, 0.5, 0.1)$. The gray line corresponds to the undisturbed case.

the airfoil massively enhances separation, resulting in the reduction of the lift over $0 < t < 1$. In contrast, the negative vortex disturbances first decrease the lift and then transiently recover it toward the undisturbed value. For both positive and negative cases, the fluctuation level is much larger compared with the undisturbed case. The majority of the lift force excitation occurs within a very short duration of two convective time units ($-1 < t < 1$).

Regarding the timing of lift excitation, the secondary negative peak for the positive gust case shifts earlier in time when a stronger gust occurs. This is due to the interaction between a vortex gust and the pre-existing negative vorticity on the suction side of the airfoil. The relationship between the signs of a vortex gust and the vorticity near the wing has been recognized as an important factor in determining the interaction pattern and load fluctuation level [26]. As observed with the spanwise-averaged spanwise vorticity snapshots at $t = -0.10$, a stronger interaction with $G = 3$ generates a larger negative ω_z near the wing. The leading-edge vortex with $G = 3$ has been completely pinched off due to the stronger gust by $t = 1$, whereas the same flow structure is still quite close to the wing at $G = 1$. This leads to a greater and faster drop in lift with $G = 3$ compared with the case with $G = 1$. This observation of timing shift in lift coincides with the case of two-dimensional, laminar vortex-gust airfoil interactions [15,27]. We note that the dynamical behavior of transient interactions with $|G| \geqslant 4$ differs from what we observe here, which is discussed in Sec. III C.

2. *The effect of vortex-impingement timing on the wing*

As the current undisturbed baseline flow exhibits unsteady separated wake while producing lift oscillation, the timing of when a vortex gust impinges on a wing may affect the dynamics. To examine this point, we consider four different timings (phases) to introduce a vortex gust with a representative case of $(G, D, Y) = (2, 0.5, 0.1)$, as shown in Fig. 6. Here, these time instants correspond to phase $\theta = \tan^{-1}(\dot{C}_L(t)/C_L(t))$ of $0, \pi/2, \pi$, and $3\pi/2$ of the current lift dynamics [28]. There are no significant differences in the dynamical behavior and the amplitude of excitation of the lift. This is because the extreme fluctuation level is significantly higher than the baseline level due to the present vortex-airfoil interaction with $|G| > 1$. Based on this observation, we hereafter consider gusts introduced at the timing at $\theta = 0$ only for the present analysis.

3. *The effect of gust orientation Y*

The vertical position of gust Y also affects the transient dynamics because it determines how the vortex gust interacts with the pre-existing vortical structures around a wing. The dependence of the extreme aerodynamic response on the vortex position Y is also investigated. We consider three vertical positions of $Y = (-0.3, -0.1, 0.1)$ for a fixed gust size of $D = 0.5$ with positive and negative gust ratios of $|G| = 2$, respectively, presented in Figs. 7 and 8. For the positive gust, the lift excitation for $Y = -0.3$ from the undisturbed case is less than that for $Y = \pm 0.1$ over

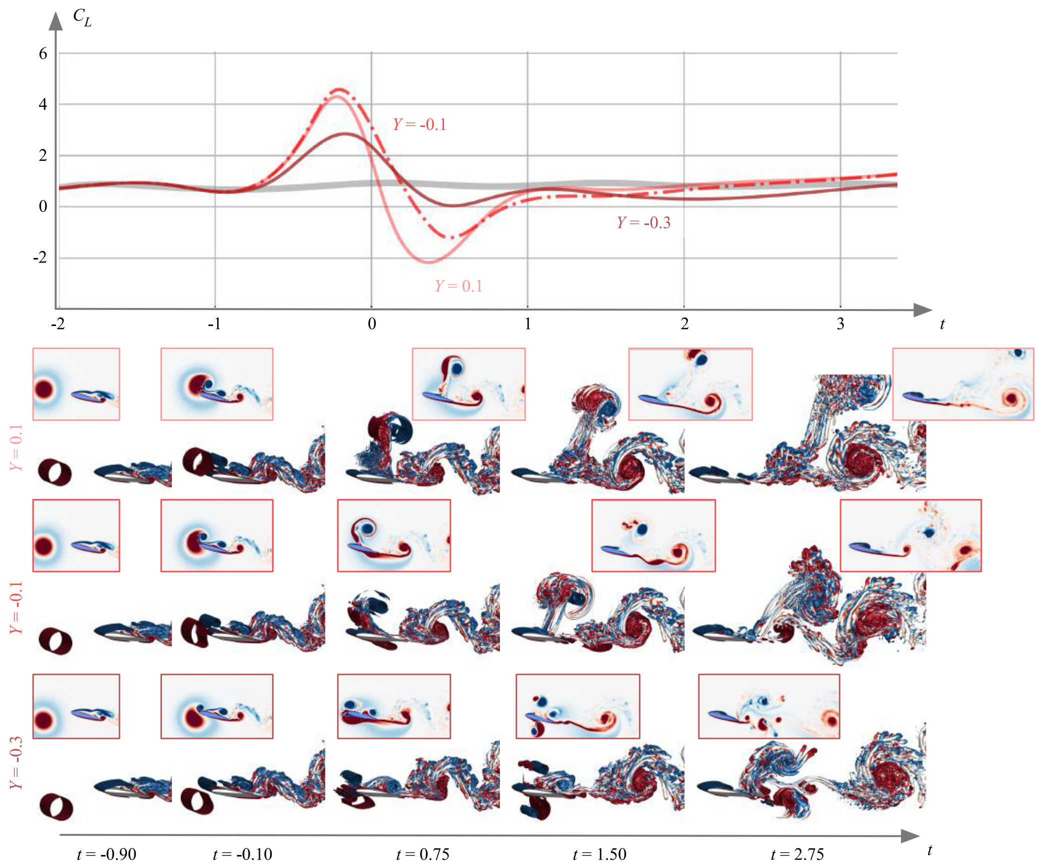

FIG. 7. Dependence of lift coefficient C_L and flow field on the initial vertical position Y for the cases of positive vortex gust. Three-dimensional flow fields visualized by the isocontours of Q-criterion and spanwise-averaged spanwise vorticity fields ω_z are presented over time. The cases for $(G, D) = (2, 0.5)$ with $Y = -0.3, -0.1$, and 0.1 are shown. The gray line in the lift response corresponds to the undisturbed case.

time. Regarding the first peak at $t \approx -0.2$, the reason for the smaller fluctuation is likely that a large portion of the positive gust interacts around the pressure side of the wing. This suggests that the excitation of lift force due to extreme-vortex gust airfoil interactions could be suppressed by performing actuation to shift the vertical location of vortex gusts.

The secondary peak observed over $0.3 < t < 0.5$ is greatly suppressed for $Y = -0.3$ compared with that for $Y = \pm 0.1$, as shown in Fig. 7. While the drastic separation due to the vortex-airfoil interaction mainly occurs above the wing for $Y = \pm 0.1$, the flow fields of $Y = -0.3$ exhibit that the separation happens at both pressure and suction sides, and the wing splits the gust. Due to these split structures at both sides of the wing, positive and negative contributions to lift eventually cancel out with each other, resulting in the suppression of lift fluctuation.

The lift fluctuation from the undisturbed response for the negative vortex cases also varies depending on the vortex position, similar to the cases with positive gusts. For the first peak of lift at $t \approx -0.1$, a smaller fluctuation is observed for $Y = 0.1$ compared with the cases of $Y = -0.1$ and -0.3 since the bottom portion of the negative gust impinges on the airfoil. The case for $Y = -0.1$ shows the largest fluctuation while exhibiting a sharp response in lift around $t = 0.75$. Similar to the positive vortex case for $Y = -0.1$, the negative gust is split by impinging on the airfoil. These split structures originated from the negative gust interaction merge with the pre-existing vortical

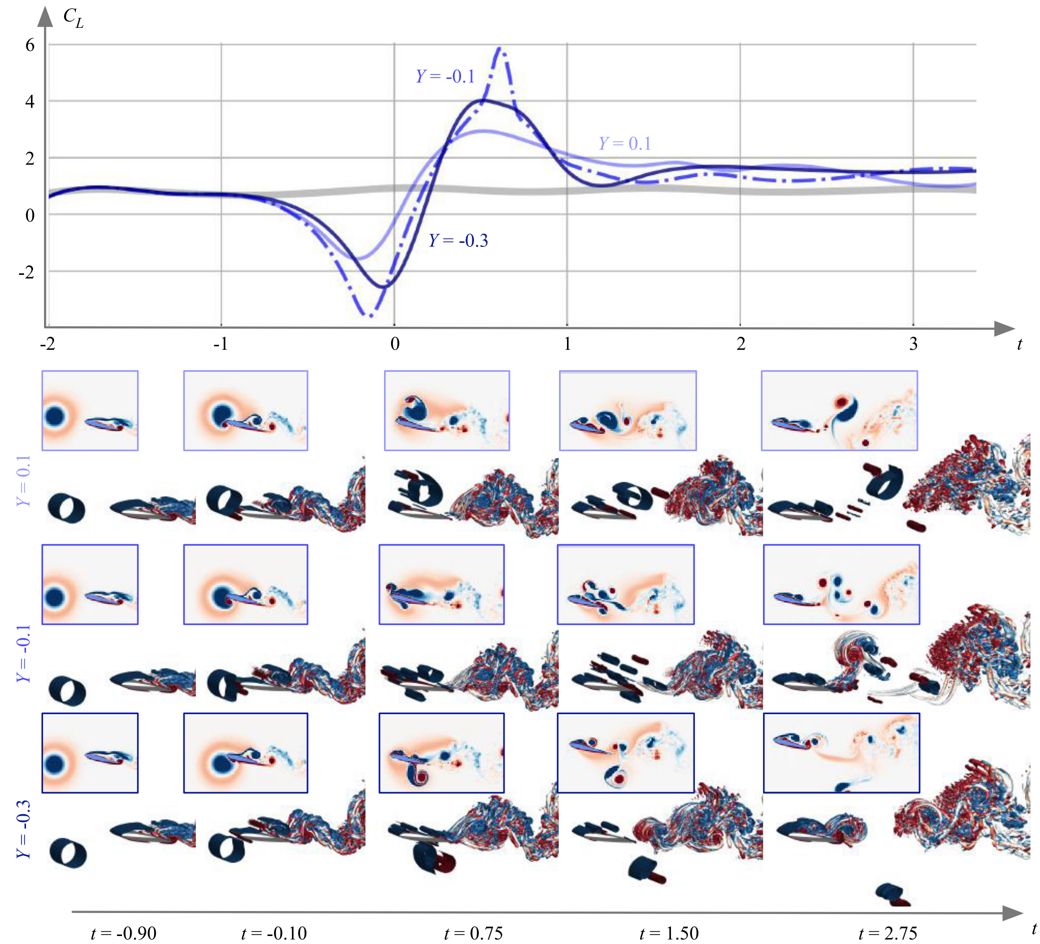

FIG. 8. Dependence of lift coefficient C_L and flow field on the initial vertical position Y for the cases of negative vortex gust. Three-dimensional flow fields visualized by the isocontours of Q-criterion and spanwise-averaged spanwise vorticity fields ω_z are presented over time. The cases for $(G, D) = (-2, 0.5)$ with $Y = -0.3, -0.1$, and 0.1 are shown. The gray line in the lift response corresponds to the undisturbed case.

structures with a negative spanwise vorticity at the suction side, as shown in Fig. 8. The resulting structures from the interaction reside around a wing at $t = 0.75$ producing a sharp lift response. Through the interaction, a set of small, two-dimensional structures is formed as seen around the suction side at $t = 1.5$. For $Y = -0.3$, the negative vortex gust mainly interacts with structures around the pressure side of a wing possessing the positive vorticity ω_z. As a result, the separating structures convect toward the bottom right in the flow field.

4. The effect of gust size D

The dependence of the extreme aerodynamic response on the gust size is also investigated. For comparison, we consider the gust ratio and vertical position of $(|G|, Y) = (2, 0.1)$ while varying the gust size D from 0.5 to 1.5. The cases with a positive vortex gust are presented in Fig. 9. Across different D, all lift histories exhibit a consistent trend of first increasing and then decreasing toward the undisturbed response. The first lift peak appears earlier as the gust size increases since a larger vortex gust reaches the wing earlier. The size of newly generated structures from the trailing

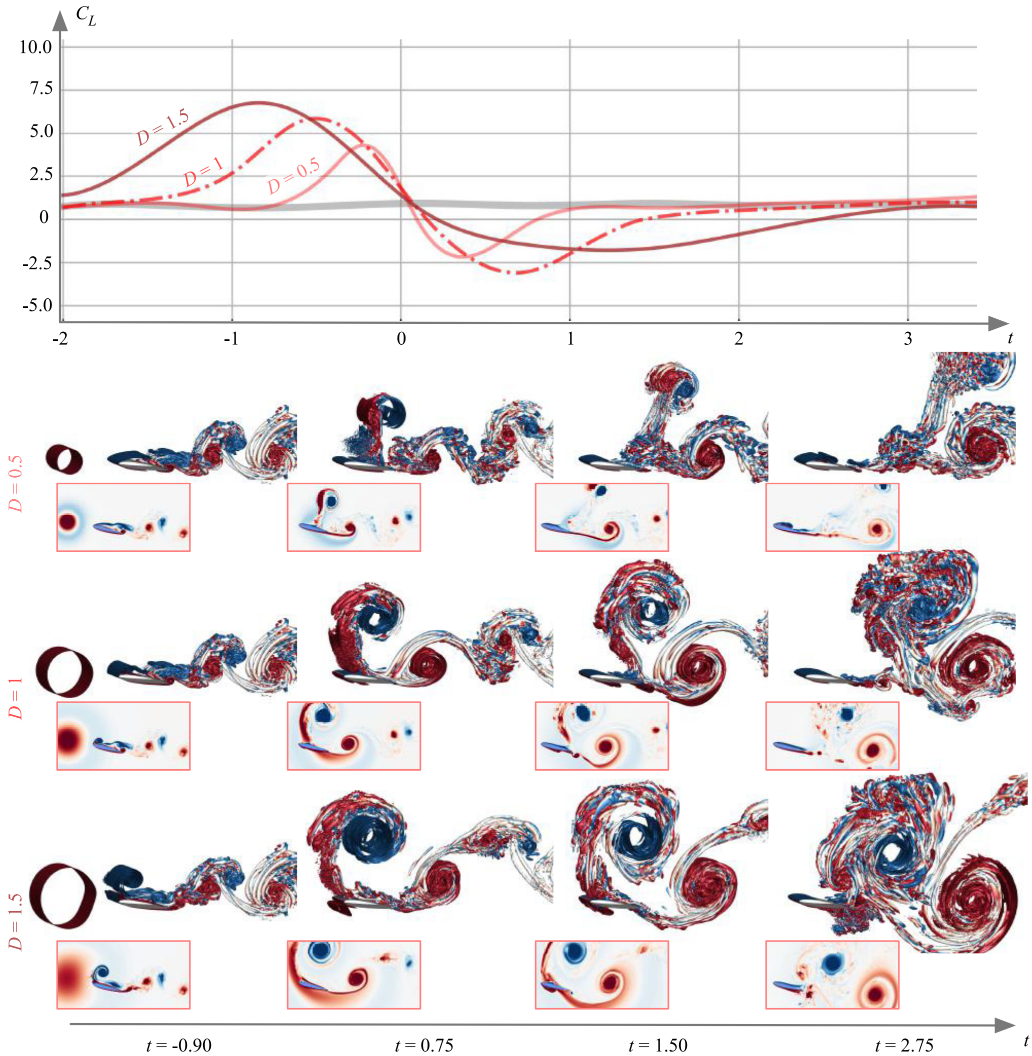

FIG. 9. Dependence of lift coefficient C_L and flow field on the gust size D for the cases of positive vortex gust. Three-dimensional flow fields visualized by the isocontours of Q-criterion and spanwise-averaged spanwise vorticity fields ω_z are presented over time. The cases for $(G, Y) = (2, 0.1)$ with $D = 0.5$, 1, and 1.5 are shown. The gray line in the lift response corresponds to the undisturbed case.

edge becomes larger with the gust size D. While the separating structure with $D = 0.5$ around the suction side simply convects over time, these newly-generated large structures from both leading and trailing edges interact with each other downstream, as shown with the flow fields at $0.75 < t < 2.75$ in Fig. 9, producing large fluctuation of lift coefficient. Because of such a large-scale interaction, the case for $D = 1.5$ takes much longer to recover the lift response toward the original level of the undisturbed lift compared with that for $D = 0.5$ and 1.

The cases with negative vortex gust varying the gust size D are depicted in Fig. 10. Similar to the observation of the positive gust cases, the impact of vortex gust appears earlier as the gust size increases. The main difference from the positive gust cases is that the lift dynamics after impinging a negative gust of $D = 1$ and 1.5 do not monotonically come back to the undisturbed trajectory. For $D = 0.5$, the gust mainly interacts with the pre-existing structure on the suction side. By increasing

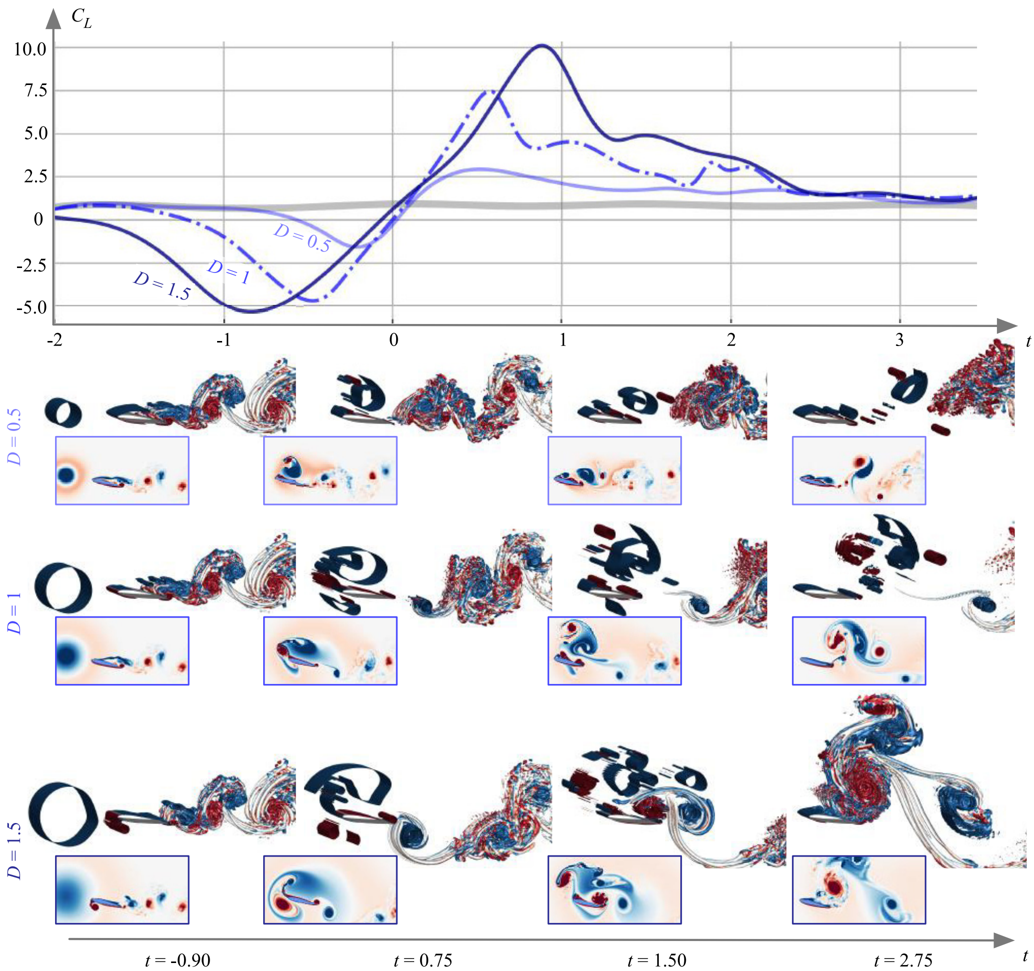

FIG. 10. Dependence of lift coefficient C_L and flow field on the gust size D for the cases of negative vortex gust. Three-dimensional flow fields visualized by the isocontours of Q-criterion and spanwise-averaged spanwise vorticity fields ω_z are presented over time. The cases for $(G, Y) = (-2, 0.1)$ with $D = 0.5$, 1, and 1.5 are shown. The gray line in the lift response corresponds to the undisturbed case.

the gust size to $D = 1$, a gust induces the generation of new structures at the pressure side, as seen at $t = 0.75$ in Fig. 10. This newly-generated structure and the upper side of the vortex gust merge and mix together above the airfoil while moving downstream, as presented with the flow fields for $t > 1.50$. A further larger gust of $D = 1.5$ also causes the generation of new structures around the pressure side at $t = 0.75$. However, since the size of this generated structure around the pressure side is enlarged as the gust size increases, the presence of this large structure induces a complicated interaction above the wing while exhibiting another interaction of large vortices near the trailing edge at $t = 1.50$. These structures, through two different vortex interactions, eventually merge with each other, producing large-scale vortical structures at $t = 2.75$. Since the interaction process is different and becomes complex as the gust size increases, the lift response with a larger gust starts to show nonmonotonic decay toward the undisturbed dynamics.

It is also worth discussing that the negative cases with $D \geqslant 1$ shown in Fig. 9 exhibit fewer three-dimensional flow characteristics over time, producing fewer fine-scale structures, compared with the positive cases shown in Fig. 10. This suggests that the negative sizable gusts suppress the spanwise instabilities that trigger the generation of three-dimensional vortical structures, which is clearly seen for $t > 0.75$ in Figs. 9 and 10. This is likely because the negative vortex gust weakens the shear layer above the wing by reducing the velocity difference between the freestream and the separated flow. Hence, the occurrence of shear layer instabilities is suppressed and delayed with the negative gusts. In contrast, the positive gust enhances separation and amplifies the shear layer instabilities, promoting early transition to turbulent vortex structures in the wake. As a result, the lift fluctuation of negative cases is larger than that of positive cases due to the absence of three-dimensional structures. Summarizing, these negative, sizable extreme gusts, preserving the two-dimensionality of the flow field, may be regarded as the most dangerous, hindering the stable flight of small-sized aircraft. Note that the lift fluctuation for $(|G|, D) = (2, 1.5)$ is even greater than the cases for the smaller size of gusts with $|G| \geqslant 4$ discussed later in Sec. III C.

B. Scale-decomposition analysis of extreme vortex-airfoil interactions

The present extreme vortex-airfoil interactions can also be examined through energy transfer across a range of spatial length scales. To do so, let us consider the scale-decomposition analysis for turbulent separated wake proposed by Fujino *et al.* [29]. We apply a spatial band-pass filter to the velocity field $\boldsymbol{u}$ based on a two-dimensional Gaussian kernel G in the x and y directions with the length scale range between σ_1 and σ_2. The operation is described as

$$\boldsymbol{u}^{[\sigma_1,\sigma_2]}(x, y, z, t) = \int_{\mathcal{S}} \boldsymbol{u}(x, y, z, t)[G(x', y'; x, y, \sigma_1) - G(x', y'; x, y, \sigma_2)]dx'dy', \tag{2}$$

where

$$G(x', y'; x, y, \sigma) = \frac{1}{2\pi\sigma^2} \exp\left[-\frac{(x-x')^2 + (y-y')^2}{2\sigma^2}\right], \tag{3}$$

and $\mathcal{S}$ denotes the integration window covering the whole computational domain in the x and y directions. Once the flow fields are decomposed in this manner, the energy transfer between the length scales can be quantified based on the decomposed flow fields.

First, the isocontours of Q-criterion obtained from the scale-decomposed flow fields for a length scale range of $[\sigma_1, 2\sigma_1]$ with $\sigma_1 = (\sigma_{\max}, \sigma_{\max}/4, \sigma_{\max}/16)$ are shown in Fig. 11. Here, the cutoff length scale is $\sigma_{\max} = c/(2\pi \mathrm{St})$, where St is the Strouhal number, corresponding to the diameter of the shed roller vortices [30]. We consider the baseline flow and a disturbed case with $(G, D, Y) = (2, 0.5, 0.1)$. For the undisturbed flow, the dominant, coherent roller vortices of wake shedding and the rib structures surrounding the vortex cores are successfully decomposed.

The scale-decomposition technique captures how the effect of a vortex gust transfers across the length scale in a transient manner for the disturbed flow. At $t = -0.70$, the cylinder-like vortex tube corresponding to the gust is seen for $\sigma_1 = (\sigma_{\max}$ and $\sigma_{\max}/4)$ while not appearing for $\sigma_1 = \sigma_{\max}/16$ since the gust itself does not possess small length scales. Once the gust impinges on the wing, fine-scale structures with $\sigma_1 = \sigma_{\max}/16$ appear at $t = 0.05$. The presence of such small length scales is also noticeable at $t = 0.80$. While the scale-decomposed field for $\sigma_1 = \sigma_{\max}$ only highlights the dominant vortex cores, structures with fine length scales are observed in the area between the wing and the massively separating structure rolled up from the leading edge. These fine-scale structures largely contribute to energy transfer dynamics, which are discussed later using the formulation in Eq. (4).

Furthermore, the effect of transient gust encounters on a range of spatial length scales can be quantified in terms of of scale-independent energy transfer of vortex stretching. Here, the energy transfer due to the vortex stretching from a provider scale σ_p to a receiver scale σ_r is defined as

$$E(\sigma_p \to \sigma_r) = \omega_i^{(\sigma_r)} S_{ij}^{(\sigma_p)} \omega_j^{(\sigma_r)} \sigma_r^2, \tag{4}$$

where the vorticity ω and the strain-rate tensor S are evaluated by the scale-decomposed velocity field with the length scales of σ_p and σ_r. This energy transfer approximately quantifies the contribu-

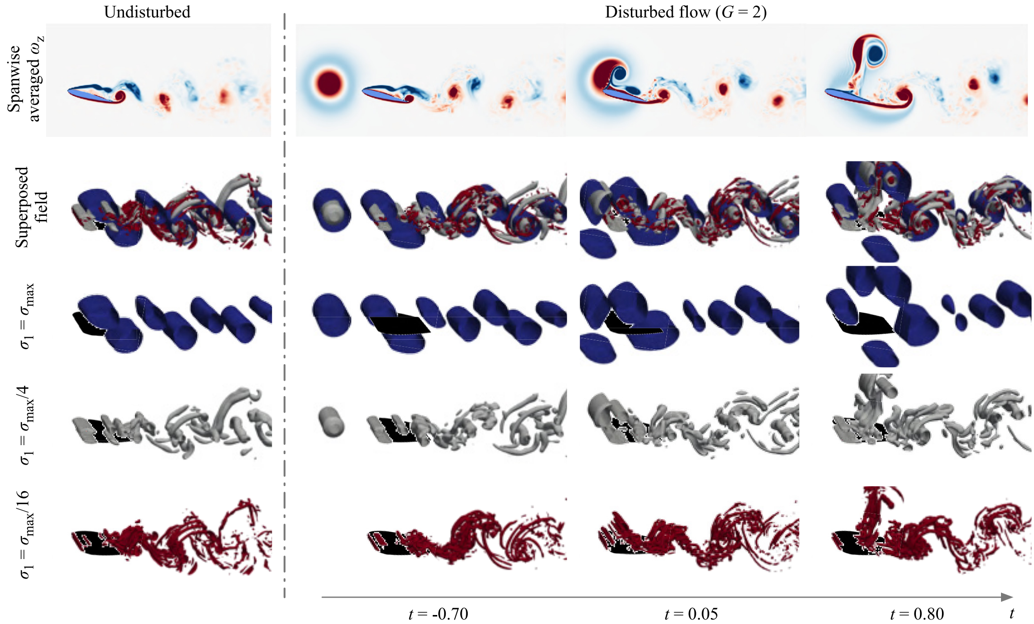

FIG. 11. Scaled-decomposed fields of the undisturbed flow and a disturbed flow of $(G, D, Y) = (2, 0.5, 0.1)$ visualized by the isocontours of Q-criterion.

tion to the stretching of vorticity at the receiver scale σ_r from strain-rate fields at the provider scale σ_p [29,31].

The energy transfer fields of the undisturbed flow and a disturbed flow of $(G, D, Y) = (2, 0.5, 0.1)$ are shown in Fig. 12. The size of structures in the field for each length scale correspondingly varies across a length scale of interest, indicating that the energy transfer captures events associated with a particular length scale. As the energy transfer considered here highlights how the energy is given or sent across a length scale due to vortex stretching, both the fields with $(\sigma_p, \sigma_r) = (\sigma_{max}, \sigma_{max}/4)$ and that with $(\sigma_p, \sigma_r) = (\sigma_{max}/4, \sigma_{max}/16)$ show strong values near the shear layers rather than the vortex cores. This is also evident from the visualization of the superposition of the spanwise-averaged magnitudes of spanwise vorticity $|\omega_z|$ and energy transfer $|E|$, depicted in Fig. 12.

For the disturbed case, the energy transfer field across a length scale varies over time. While both the gust and the region near the leading edge do not show high E at $t = -0.70$, a strong energy transfer between a small-length-scale range of $(\sigma_p, \sigma_r) = (\sigma_{max}/4, \sigma_{max}/16)$ is observed for $t > 0.05$ due to the interaction between the gust and wing. In other words, the energy from large-scale structures, including a gust, is given to small length scales that emerge due to the transient extreme vortex-airfoil interaction.

C. Extreme vortex-airfoil interactions with $|G| \geqslant 4$

While the primary feature of lift responses and flow fields is two-dimensional up to the gust ratio $|G|$ of 3, the aerodynamic response becomes different when a wing encounters a much stronger gust. Here, we consider the cases for $G = \pm(4, 5)$ with $(D, Y) = (0.5, 0.1)$, as shown in Fig. 13. The lift increases or decreases with a positive or negative gust when a gust approaches the wing over $-1 < t < 0$, similar to the cases with $|G| \leqslant 3$. For the positive case, once the gust induces drastic separation at the leading edge, the separating structure rotates above the wing (as seen at $t = 0.75$) and impinges on the wing again at $t \approx 1.50$ for $G = 4$ and $t \approx 1.05$ for $G = 5$. Correspondingly, the lift coefficient drastically increases again at $t \approx 1$ before converging to the level of undisturbed

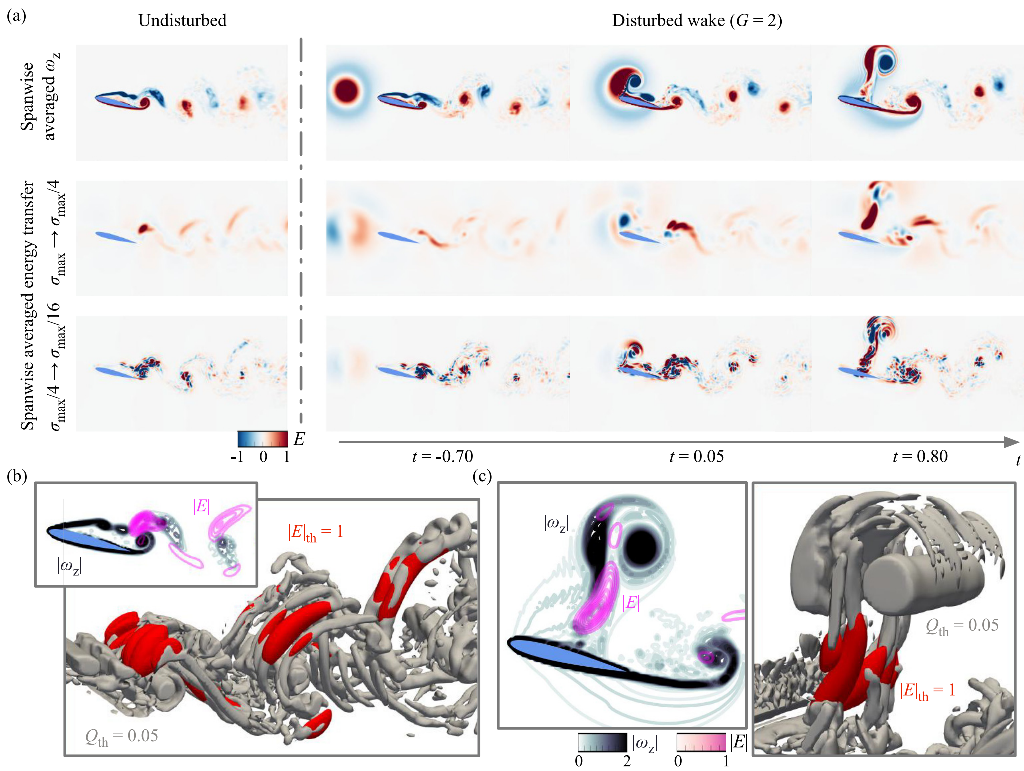

FIG. 12. Scale-independent energy transfer of extreme vortex-airfoil interactions. (a) Spanwise-averaged energy transfer field of the undisturbed flow and a disturbed flow of $(G, D, Y) = (2, 0.5, 0.1)$. Superposition of the spanwise-averaged magnitudes of spanwise vorticity $|\omega_z|$ and energy transfer $|E|$, and that of the isocontours of Q-criterion and energy transfer, with $(\sigma_p, \sigma_r) = (\sigma_{\max}, \sigma_{\max}/4)$ are shown for (b) the undisturbed flow and (c) the disturbed flow at $t = 0.80$.

lift response. After the second impingement for $t > 1.5$, fine-scale structures emerge and interact with the wake across the convection process.

We note that the emergence of fine structures might be triggered before the second impingement occurs. According to snapshots at $t \approx 1.50$ for $G = 4$ and $t \approx 1.05$ for $G = 5$, the vortex pair bounding above the wing becomes unstable right before arriving at the wing surface. Hence, the three-dimensionality observed here may be caused by the interaction between the wing, gust, and small-scale structures newly produced during the transient process.

For the negative case, once the gust induces separation at $t = 0.75$, the separating structure jumps downstream and immediately merges with the wake. This is contrary to the cases with $G \leqslant 3$, for which the gust convects while interacting with vortical structures near the wing. Analogous to the positive cases, fine-scale structures are observed due to the mixing of the wake and the separating structures, as seen at $t = 2.50$ in Fig. 12. While both positive and negative strong gusts with $|G| \geqslant 4$ trigger spanwise instabilities, the timing of appearance for three-dimensional fine-scale structures depends on the sign and magnitude of gusts, causing the difference in the interaction between transient vortical structures and wake.

D. Data-driven compression of extreme aerodynamic flows

Through the previous computational analysis, we revealed that extreme vortex-airfoil interaction in a three-dimensional domain still preserves the two-dimensionality of flow and lift responses for $|G| \lesssim 3$. In a previous study, we found that a collection of vorticity data for two-dimensional

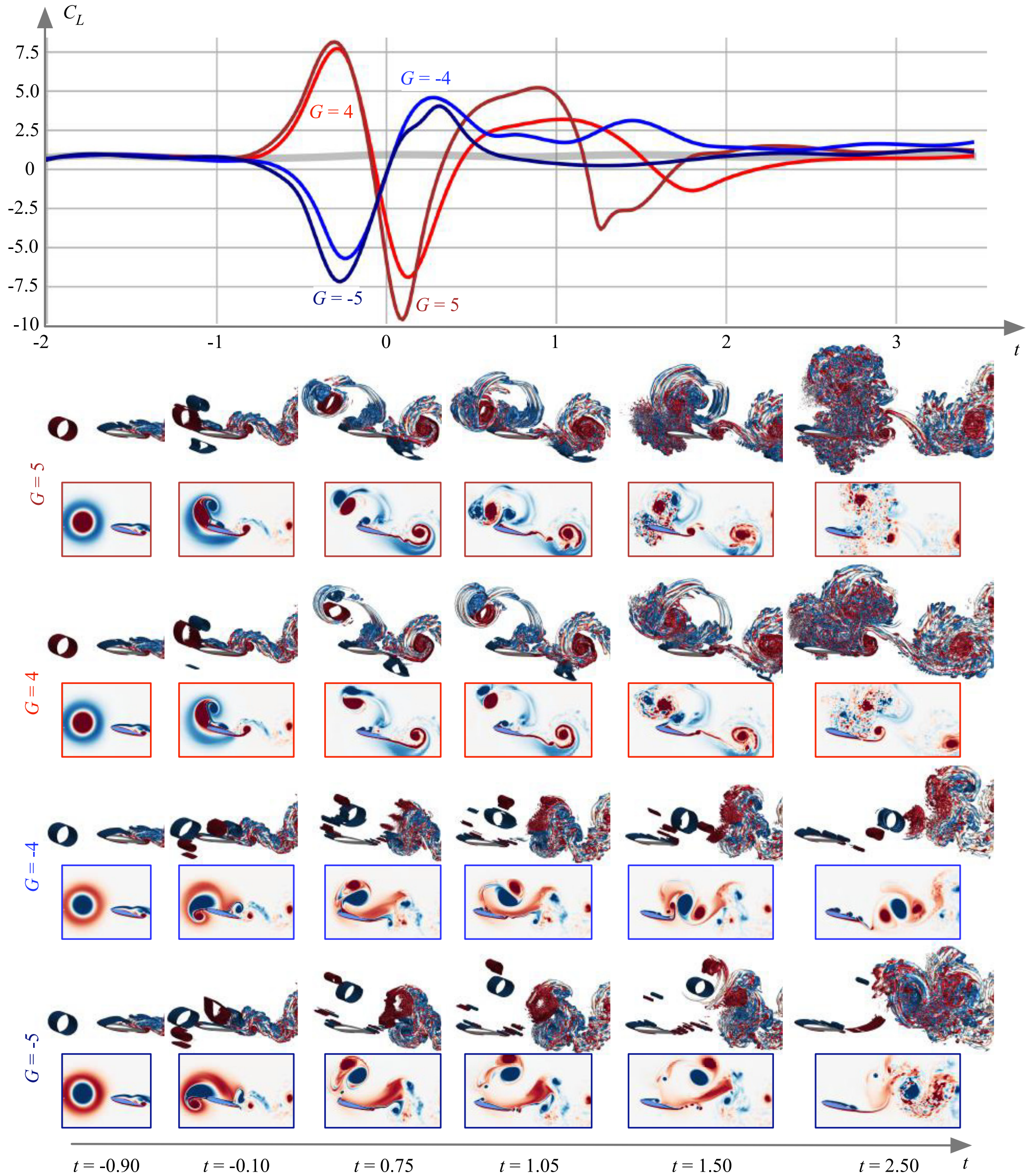

FIG. 13. Extreme vortex-airfoil interaction with $G = \pm 4$ and ± 5 for $(D, Y) = (0.5, 0.1)$. Three-dimensional flow fields visualized by the isocontours of Q-criterion and spanwise-averaged spanwise vorticity fields ω_z are presented over time. The gray line in the lift response corresponds to the undisturbed case.

extreme vortex-airfoil interaction over time and parameter space at $\mathrm{Re} = 100$ can be compressed into three variables using nonlinear machine learning [15]. Based on the discovery of a low-rank nature of two-dimensional extreme aerodynamic flows, we pose the question of whether the current extreme vortex-airfoil interactions at $\mathrm{Re} = 5000$ can also be described with a few variables. Here, we consider unsupervised data-driven compression for the present datasets of extreme aerodynamic flows with $|G| \leqslant 3$.

An observable-augmented nonlinear autoencoder [15] is used for the present compression, as illustrated in Fig. 14. An autoencoder [32,33] is a neural-network-based order-reduction technique,

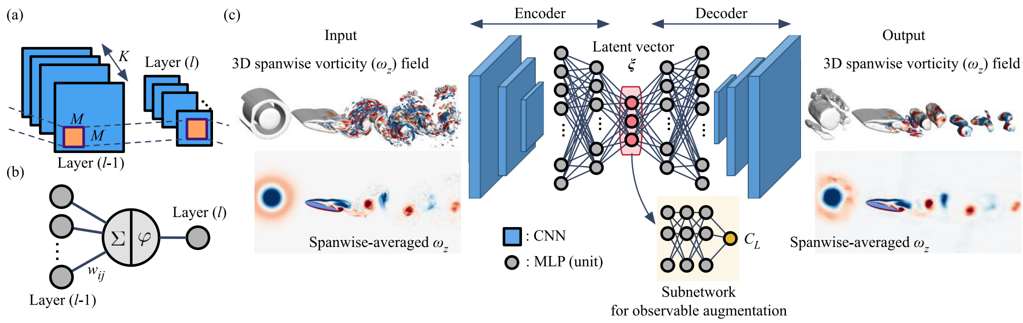

FIG. 14. Data-driven compression of extreme aerodynamic flows. (a) Convolutional layer inside convolutional neural networks. (b) A perceptron, a minimum unit of multilayer perceptron. (c) Observable-augmented nonlinear autoencoder.

which takes the same data as the input and output of the model. The autoencoder model is composed of an encoder $\mathcal{F}_e$ and a decoder $\mathcal{F}_d$ while possessing the bottleneck called the latent vector $\boldsymbol{\xi}$ whose data dimension is generally set to much lower than that of the input and output. Hence, a given input data $\boldsymbol{q}$ can be compressed into the latent vector $\boldsymbol{\xi}$ if the autoencoder successfully reconstructs the original data. These encoding and decoding processes are expressed as

$$\boldsymbol{q} \approx \mathcal{F}(\boldsymbol{q}) = \mathcal{F}_d(\mathcal{F}_e(\boldsymbol{q})), \quad \boldsymbol{\xi} = \mathcal{F}_e(\boldsymbol{q}), \quad \boldsymbol{q} \approx \hat{\boldsymbol{q}} = \mathcal{F}_d(\boldsymbol{\xi}), \tag{5}$$

where $\hat{(\cdot)}$ represents a reconstructed variable.

Our previous study showed that low-dimensional representations $\boldsymbol{\xi}$ obtained through a nonlinear autoencoder can capture the aerodynamic characteristics of extreme vortex-airfoil interaction by incorporating the lift coefficient $C_L(t)$ into the learning formulation. The present model, referred to as an observable-augmented autoencoder, includes the additional branch subnetwork connected with the latent variables $\boldsymbol{\xi}(t)$, as illustrated by the yellow-shaded portion in Fig. 14, outputting $C_L(t)$. The optimization for the weights inside the lift-augmented autoencoder is performed with

$$\boldsymbol{w}^* = \mathrm{argmin}_{\boldsymbol{w}}[||\boldsymbol{q} - \hat{\boldsymbol{q}}||_2 + \beta||C_L - \hat{C}_L||_2], \tag{6}$$

where β balances the vorticity field and lift reconstruction loss terms. We choose $\beta = 0.05$ based on the L-curve analysis [34] that finds an appropriate regularization parameter of the cost function. Since the lift coefficient needs to be accurately estimated to minimize the loss function, this formulation enables $\boldsymbol{w}$ to be tuned to capture important vortical structures correlated with the lift coefficient due to $\Gamma \propto C_L$, where Γ is circulation. This augmentation also promotes capturing large transient lift caused by the present extreme vortex-airfoil interactions. The observable-augmented network has been used in a range of aerodynamic examples, such as flow control design [16,17], shape optimization of electric vehicles [35], and sensor-based global field reconstruction [36–39].

The present observable-augmented autoencoder composed of a multilayer perceptron [40] and a convolutional neural network [41] is trained using the cases with $G = \pm(1, 2, 3)$ for $(D, Y) = (0.5, 0.1)$ and the undisturbed flow. Each case includes 110 snapshots collected over 5.5 convective time. A subdomain of $(x, y, z)/c \in [-1.5, 4.5] \times [-1.5, 1.5] \times [0, 1]$ is extracted from the computational domain for the present data-driven analysis. We interpolated datasets onto a Cartesian, uniform grid with spatial grid points $(N_x, N_y, N_z) = (300, 150, 50)$ to use them for the present convolutional neural network-based autoencoder. To examine how the autoencoder learns the three-dimensionality of the flows through nonlinear compression, we consider a three-dimensional and a spanwise-averaged vorticity field ω_z as a variable of interest. We use 70% of the datasets for training, and the remaining 30% are prepared for validation. For the training process of the observable-augmented autoencoder, early stopping [42] with the criterion of a series of continuous

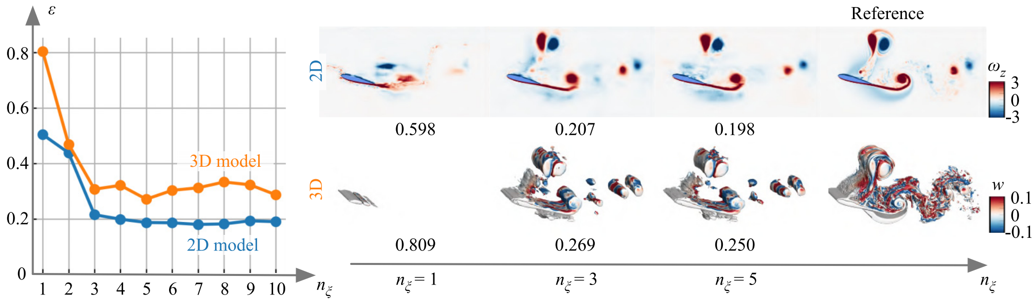

FIG. 15. Dependence of the reconstructed vorticity field on the latent dimension size n_ξ. The disturbed flow for $(G, D, Y) = (2, 0.5, 0.1)$ is shown as a representative case. The L_2 reconstruction error ε is reported underneath each contour. For the three-dimensional case, the isocontour of ω_z is colored by the spanwise velocity w.

100 epochs is employed to avoid overfitting. Details on the autoencoder formulation are provided in Fukami and Taira [15].

To observe how much the present extreme aerodynamic flows can be nonlinearly compressed through the observable-augmented autoencoder, the dependence of the reconstructed vorticity field on the latent dimension n_ξ is examined, as shown in Fig. 15. The error decreases as the size of the latent vector increases for both two- and three-dimensional models. The error plateaus for $n_\xi \geqslant 3$, suggesting that the primary feature of the present extreme aerodynamic flows can be expressed with three-dimensional variables. This coincides with the finding of the three-dimensional latent space in a previous study [15]. The reason for the higher error of the three-dimensional model compared with that of the two-dimensional model is discussed with the results in Fig. 18.

The decoded vorticity field and lift coefficient through the two-dimensional model with $n_\xi = 3$ are presented in Fig. 16. Here, we define the L_2 reconstruction error $\varepsilon = ||\boldsymbol{q} - \hat{\boldsymbol{q}}||_2/||\boldsymbol{q}||_2$. The present nonlinear autoencoder reasonably reconstructs vortical structures of the undisturbed case

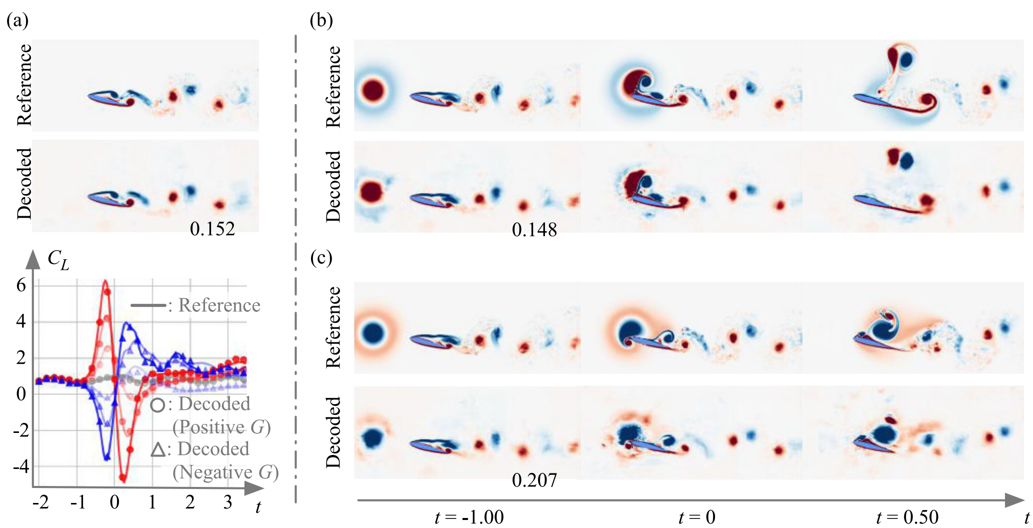

FIG. 16. Reconstructed vorticity fields with the two-dimensional model for (a) the undisturbed and the disturbed cases, (b) $G = 2$ and (c) -2. For the three-dimensional case, the isocontour of ω_z is colored by the spanwise velocity w. The estimated lift coefficient from the subnetwork is also shown.

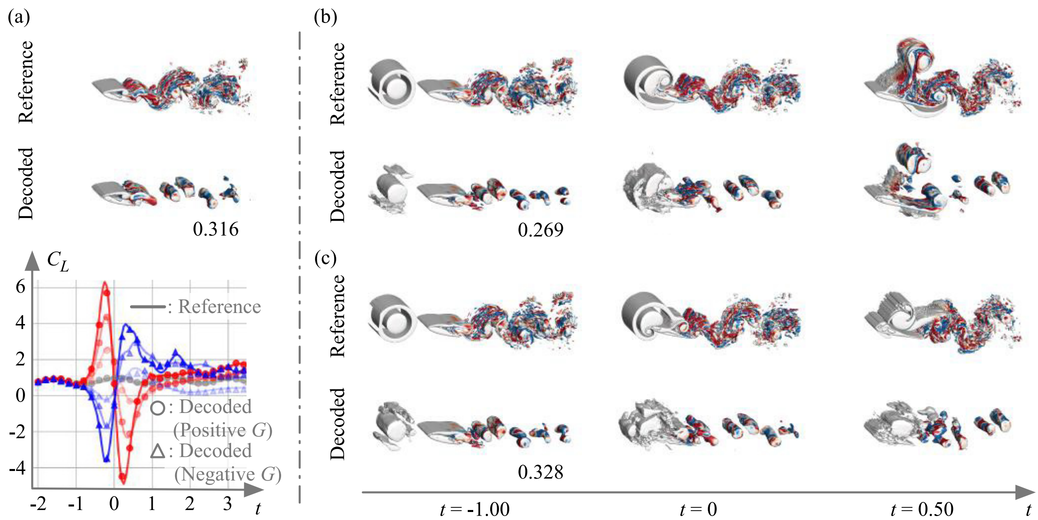

FIG. 17. Reconstructed vorticity fields with the three-dimensional model for (a) the undisturbed and the disturbed cases, (b) $G = 2$ and (c) -2. For the three-dimensional case, the isocontour of ω_z is colored by the spanwise velocity w. The estimated lift coefficient from the subnetwork is also shown.

and represents the transient gust-airfoil interaction process of the disturbed cases. Accurate estimation of the lift coefficient also suggests that the high-dimensional data of extreme vortex-airfoil interaction can be compressed into only three variables while extracting the important vortical structures associated with lift.

The reconstruction results with the three-dimensional model tell us how the present nonlinear lift-augmented autoencoder learns the relationship between the vortical structures and lift coefficients through the compression process. The decoded vorticity field and lift coefficient for the three-dimensional model with $n_\xi = 3$ are presented in Fig. 17. Interestingly, the three-dimensional decoded fields retain only the vortex cores similar to structures captured by the scale-decomposition analysis for $\sigma_1 = c/(2\pi \mathrm{St})$ while discarding small-scale structures through the nonlinear compression process. While a regular autoencoder may also discard fine-scale structures as well due to its compression process, the accurate lift estimation indicates that the large-scale information compressed in the present low-order subspace is sufficient to estimate the lift. In other words, although losing small scales itself is not due to the lift-based augmentation, it can be argued that these dominant vortex cores primarily contributing to estimating lift are extracted into the three-dimensional latent variables through the lift-augmented nonlinear autoencoder. This observation is similar to a finding in a recent study examining the extraction of dominant vortical structures for lift dynamics through an information-theoretic approach [43].

To further discuss the point regarding the extraction of primary two-dimensional features through nonlinear compression, the spanwise-averaged reconstructed fields with the three-dimensional model are shown in Fig. 18. Since the three-dimensional model retains the dominant vortex cores as presented in Fig. 17, the spanwise-averaged field that smooths out fine structures is in agreement with the reference data. In addition, the L_2 error calculated based on the spanwise-averaged field is decreased compared with that directly obtained from the three-dimensional reconstructed field. This indicates that the higher error of the three-dimensional model observed in Fig. 15 is due to the presence of small-scale structures. In other words, both two- and three-dimensional models essentially learn the same primary features of vortical flows through the observable-augmented nonlinear compression, implying that lift response is mainly driven by two-dimensional flow mechanisms.

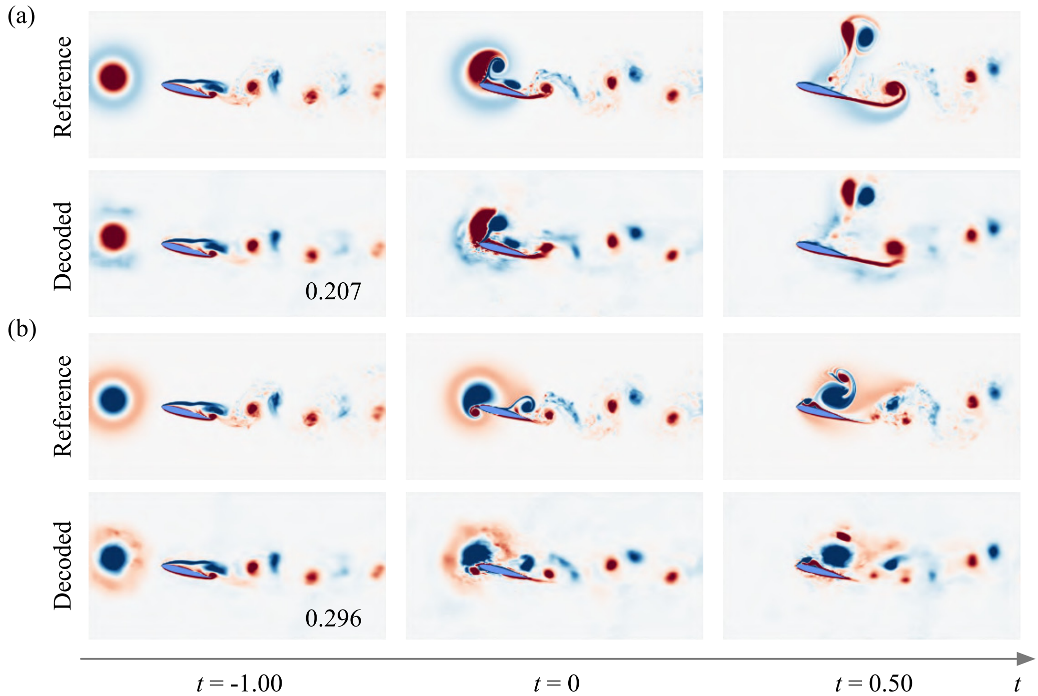

FIG. 18. Spanwise-averaged fields of the reconstruction with the three-dimensional model for the disturbed case, (a) $G = 2$ and (b) $G = -2$.

These results also suggest that the three-dimensional model learns spanwise-averaging operations through expensive neural-network training. This cautions that when developing reduced-order models of extreme vortex-airfoil interactions for conditions in which the main dynamics are still two-dimensional, performing preprocessing of data based on flow characteristics can be considered to wisely deal with datasets while saving computational costs rather than naïvely giving them into the model. The current finding regarding the low-rank nature of the current extreme vortex-airfoil interactions suggests that sparse-sensing techniques [27,36,37] and data-driven flow control strategies [16,17] that have been developed with two-dimensional problems may be considered for extreme aerodynamic flows across different Reynolds numbers.

IV. CONCLUDING REMARKS

We examined extreme vortex-gust airfoil interactions through numerical simulations and unsupervised data-driven analysis. LESs were performed on flows around an NACA0012 airfoil at a chord-based Reynolds number of 5000 and an angle of attack of 14°. An extremely strong gust with a Taylor vortex profile was introduced upstream of the wing to investigate the dependence of aerodynamic forces and vortical flows on gust parameters, including magnitude, size, rotational direction, and orientation. We found that the lift responses and flow fields present two-dimensionality up to a gust ratio $|G|$ of 3, while small-scale structures emerge with $|G| \geqslant 4$, triggering instabilities during the interaction. The fluctuation of aerodynamic loads from the undisturbed state is amplified as the gust size increases, with the large deformation of vortical flows at an earlier stage compared with small-sized gusts, highlighting the potential risks to stable flight. Furthermore, the unsteady lift response is highly influenced by the orientation of the gust and its rotational direction, offering insights into lift attenuation control.

Scale-decomposition analysis was further performed to examine the energy-transfer dynamics of extreme vortex-airfoil interactions across various spatial length scales. We showed that energy from large-scale structures, including the gust, is given to small length scales that emerge from the interaction. Based on the current findings, unsupervised learning-based data compression was also considered. With an observable-augmented nonlinear autoencoder, vortical flow snapshots with $|G| \leqslant 3$, where interaction dynamics were primarily two-dimensional, can be compressed to three variables. The low-rank nature of the extreme aerodynamic flows suggests the potential of data-driven sensing and control techniques developed with two-dimensional model problems for high-Reynolds-number scenarios.

Although this study focused on three-dimensional flow structures with a two-dimensional airfoil, the effect of extreme vortex-airfoil interaction on a three-dimensional wing should be examined in the future. The interaction between extreme gusts and structures appearing due to the three-dimensionality of the wing, such as tip vortices that significantly contribute to the lift generation, would be of interest. Comparisons between such extensions and the current findings offer further insights into extreme aerodynamic flows, potentially supporting stable flight operations for next-generation aircraft.

ACKNOWLEDGMENTS

We acknowledge support from the US Air Force Office of Scientific Research (FA9550-21-1-0178) and the US Department of Defense Vannevar Bush Faculty Fellowship (N00014-22-1-2798). This study used computational and storage services associated with the Hoffman2 Shared Cluster provided by the UCLA Institute for Digital Research and Education's Research Technology Group. Part of the machine-learning analysis was performed on a Delta GPU at the National Center for Supercomputing Applications (NCSA) through the ACCESS program (Allocation PHY230125). K.F. thanks the support from JSPS KAKENHI Grant No. JP25K23418.

DATA AVAILABILITY

The data that support the findings of this article are not publicly available upon publication because it is not technically feasible, and/or the cost of preparing, depositing, and hosting the data would be prohibitive within the terms of this research project. The data are available from the authors upon reasonable request.

APPENDIX: PRESSURE COEFFICIENT

In this appendix, we examine the time-varying pressure coefficient $C_p(t)$ on the wing surface with varying gust ratio G for cases of $(D, Y) = (0.5, 0.1)$, as shown in Fig. 19. At $t = -0.90$, when a vortex gust approaches, the pressure near the trailing edge sharply decreases regardless of the sign of the vortex gust. This is likely because both positive and negative gusts induce the local positive vorticity on the suction side near the trailing edge before the impingement. As a result, locally modified structures near the trailing edge produce strong suction, thereby reducing C_p.

The large fluctuation of lift discussed in Sec. III A 1 is evident from the pressure coefficient. Once the gust impinges on the wing at $t = -0.10$, the pressure coefficient near the leading edge greatly deviates from the undisturbed response. The fluctuation from the undisturbed baseline profile becomes larger as $|G|$ increases for $t \leqslant -0.10$. However, it is no longer ordered in magnitude of G for $t \geqslant 0.75$ while exhibiting a nonmonotonic profile of pressure coefficient due to complex interactions between a vortex gust, the pre-existing structures near the wing, and the wake. For example, the case of $G = -3$ presents larger fluctuation than that of $G = -5$ because the interaction for $G = -3$ primarily occurs near the wing, while the newly-generated vortex pair from the region near the leading edge jumps toward the wake and quickly collides with it. The flow fields and the

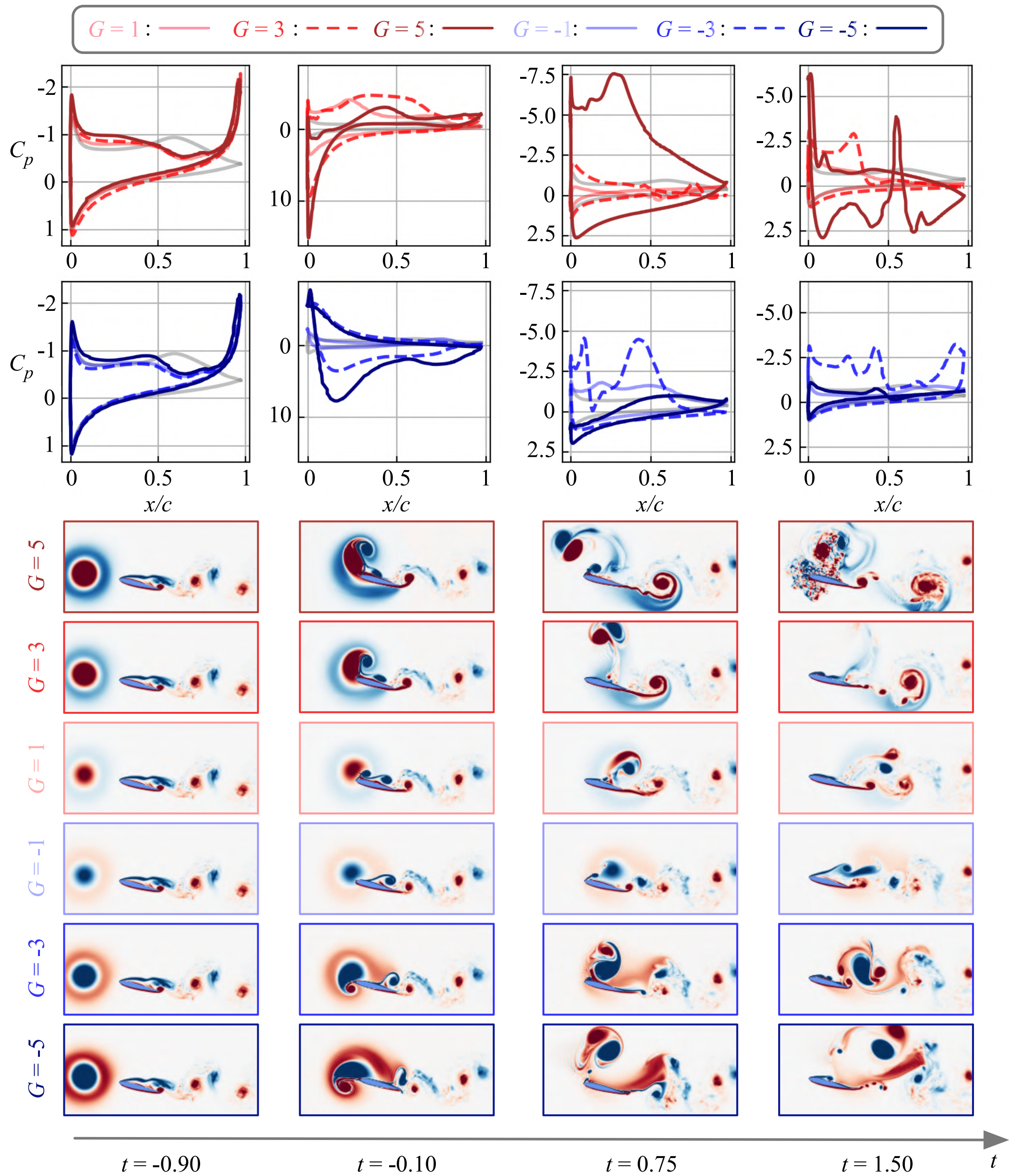

FIG. 19. Dependence of the pressure coefficient C_p on the wing surface and flow field on the gust ratio G. Spanwise-averaged spanwise vorticity fields ω_z are presented over time. The gray line in the pressure response corresponds to the undisturbed case.

local pressure distributions during extreme vortex-gust airfoil interactions are shown to provide a full description of the dynamical events.

[1] A. R. Jones, O. Cetiner, and M. J. Smith, Physics and modeling of large flow disturbances: Discrete gust encounters for modern air vehicles, Annu. Rev. Fluid Mech. **54**, 469 (2022).

[2] C. M. Stutz, J. T. Hrynuk, and D. G. Bohl, Dimensional analysis of a transverse gust encounter, Aerosp. Sci. Technol. **137**, 108285 (2023).
[3] Y. Qian, Z. Wang, and I. Gursul, Lift alleviation in travelling vortical gusts, Aeronaut. J. **127**, 1676 (2023).
[4] B. Herrmann, S. L. Brunton, J. E. Pohl, and R. Semaan, Gust mitigation through closed-loop control. II. Feedforward and feedback control, Phys. Rev. Fluids **7**, 024706 (2022).
[5] G. Sedky, A. Gementzopoulos, F. D. Lagor, and A. R. Jones, Experimental mitigation of large-amplitude transverse gusts via closed-loop pitch control, Phys. Rev. Fluids **8**, 064701 (2023).
[6] C. J. Barnes and M. R. Visbal, Counterclockwise vortical-gust/airfoil interactions at a transitional Reynolds number, AIAA J. **56**, 2540 (2018).
[7] C. J. Barnes and M. R. Visbal, Clockwise vortical-gust/airfoil interactions at a transitional Reynolds number, AIAA J. **56**, 3863 (2018).
[8] L. Smith, K. Fukami, G. Sedky, A. Jones, and K. Taira, A cyclic perspective on transient gust encounters through the lens of persistent homology, J. Fluid Mech. **980**, A18 (2024).
[9] Y. Zhong, A. Amiri-Margavi, H. Babaee, and K. Taira, Optimally time-dependent modes of vortex gust-airfoil interactions, J. Fluid Mech. **1006**, A18 (2025).
[10] A. R. Jones and O. Cetiner, Overview of unsteady aerodynamic response of rigid wings in gust encounters, AIAA J. **59**, 731 (2021).
[11] A. Moushegian and M. J. Smith, Analysis of a wing moving through a nonlinear gust, *AIAA Scitech 2019 Forum, San Diego, California* (AIAA, Reston, VA, 2019), Paper No. AIAA 2019-0637..
[12] H. Biler, G. Sedky, A. R. Jones, M. Saritas, and O. Cetiner, Experimental investigation of transverse and vortex gust encounters at low Reynolds numbers, AIAA J. **59**, 786 (2021).
[13] I. Andreu-Angulo, H. Babinsky, H. Biler, G. Sedky, and A. R. Jones, Effect of transverse gust velocity profiles, AIAA J. **58**, 5123 (2020).
[14] I. Andreu-Angulo and H. Babinsky, Controlling upwards and downwards gust loads on aerofoils by pitching, Exp. Fluids **64**, 129 (2023).
[15] K. Fukami and K. Taira, Grasping extreme aerodynamics on a low-dimensional manifold, Nat. Commun. **14**, 6480 (2023).
[16] K. Fukami, H. Nakao, and K. Taira, Data-driven transient lift attenuation for extreme vortex gust-airfoil interactions, J. Fluid Mech. **992**, A17 (2024).
[17] Z. Liu, D. Beckers, and J. D. Eldredge, Model-based reinforcement learning for control of strongly-disturbed unsteady aerodynamic flows, AIAA J. (2025), doi:10.2514/1.J064790.
[18] F. Ham and G. Iaccarino, Energy conservation in collocated discretization schemes on unstructured meshes, in *Annual Research Briefs* (Center for Turbulence Research, 2004), pp. 3–14.
[19] F. Ham, K. Mattsson, and G. Iaccarino, Accurate and stable finite volume operators for unstructured flow solvers, in *Annual Research Briefs* (Center for Turbulence Research, 2006), pp. 243–261.
[20] L. V. Rolandi, J. H. M. Ribeiro, C.-A. Yeh, and K. Taira, An invitation to resolvent analysis, Theor. Comput. Fluid Dyn. **38**, 603 (2024).
[21] L. V. Rolandi, L. Smith, M. Amitay, V. Theofilis, and K. Taira, Biglobal resolvent analysis of separated flow over a NACA0012 airfoil, arXiv:2501.04255.
[22] A. W. Vreman, An eddy-viscosity subgrid-scale model for turbulent shear flow: Algebraic theory and applications, Phys. Fluids **16**, 3670 (2004).
[23] G. I. Taylor, *On the Dissipation of Eddies* (Cambridge University Press, Cambridge, 1918), pp. 96–101.
[24] S. Gupta, J. Zhao, A. Sharma, A. Agrawal, K. Hourigan, and M. C. Thompson, Two- and three-dimensional wake transitions of a NACA0012 airfoil, J. Fluid Mech. **954**, A26 (2023).
[25] G. J. Sheard, M. C. Thompson, and K. Hourigan, Subharmonic mechanism of the mode C instability, Phys. Fluids **17**, 111702 (2005).
[26] D. Peng and J. W. Gregory, Asymmetric distributions in pressure/load fluctuation levels during blade-vortex interactions, J. Fluids Struct. **68**, 58 (2017).
[27] Y. Zhong, K. Fukami, B. An, and K. Taira, Sparse sensor reconstruction of vortex-impinged airfoil wake with machine learning, Theor. Comput. Fluid Dyn. **37**, 269 (2023).

[28] Y. Kim, V. Godavarthi, L. V. Rolandi, J. T. Klamo, and K. Taira, Influence of three-dimensionality on wake synchronisation of an oscillatory cylinder, J. Fluid Mech. **1001**, A24 (2024).

[29] J. Fujino, Y. Motoori, and S. Goto, Hierarchy of coherent vortices in turbulence behind a cylinder, J. Fluid Mech. **975**, A13 (2023).

[30] T. Yasuda, S. Goto, and J. C. Vassilicos, Formation of power-law scalings of spectra and multiscale coherent structures in the near-field of grid-generated turbulence, Phys. Rev. Fluids **5**, 014601 (2020).

[31] T. Yoneda, S. Goto, and T. Tsuruhashi, Mathematical reformulation of the Kolmogorov–Richardson energy cascade in terms of vortex stretching, Nonlinearity **35**, 1380 (2022).

[32] G. E. Hinton and R. R. Salakhutdinov, Reducing the dimensionality of data with neural networks, Science **313**, 504 (2006).

[33] K. Fukagata and K. Fukami, Compressing fluid flows with nonlinear machine learning: Mode decomposition, latent modeling, and flow control, Fluid Dyn. Res. **57**, 041401 (2025).

[34] P. C. Hansen and D. P. O'Leary, The use of the L-curve in the regularization of discrete ill-posed problems, SIAM J. Sci. Comput. **14**, 1487 (1993).

[35] J. Tran, K. Fukami, K. Inada, D. Umehara, Y. Ono, K. Ogawa, and K. Taira, Aerodynamics-guided machine learning for design optimization of electric vehicles, Comms. Eng. **3**, 174 (2024).

[36] K. Fukami and K. Taira, Data-driven modeling, sensing, and control of extreme vortex-airfoil interactions, *AIAA Aviation Forum and Ascend 2024, Las Vegas, Nevada* (AIAA, Reston, VA, 2024), Paper No. AIAA 2024-4531.

[37] H. Mousavi and J. D. Eldredge, Low-order flow reconstruction and uncertainty quantification in disturbed aerodynamics using sparse pressure measurements, J. Fluid Mech. **1013**, A41 (2025).

[38] K. Fukami and K. Taira, Observable-augmented manifold learning for multi-source turbulent flow data, J. Fluid Mech. **1010**, R4 (2025).

[39] J. D. Eldredge and H. Mousavi, A review of Bayesian sensor-based estimation and uncertainty quantification of aerodynamic flows, arXiv:2502.20280.

[40] D. E. Rumelhart, G. E. Hinton, and R. J. Williams, Learning representations by back-propagation errors, Nature (London) **323**, 533 (1986).

[41] Y. Lecun, L. Bottou, Y. Bengio, and P. Haffner, Gradient-based learning applied to document recognition, Proc. IEEE **86**, 2278 (1998).

[42] L. Prechelt, Automatic early stopping using cross validation: Quantifying the criteria, Neural Netw. **11**, 761 (1998).

[43] K. Fukami and R. Araki, Information-theoretic machine learning for time-varying mode decomposition of separated aerodynamic flows, AIAA J. (2025), doi:10.2514/1.J065914.